AGU PUBLICATIONS

JGR

Journal of Geophysical Research: Atmospheres

RESEARCH ARTICLE

10.1002/2013JD020699

Key Points:
- Relationship between clouds and dynamics in cyclones is quantified
- Relationship between clouds and dynamical variables changes with height
- The model failed to represent the observed cloud to dynamics relationship

Correspondence to:
P. Govekar,
pallavi.govekar@unimelb.edu.au

Citation:
Govekar, P. D., C. Jakob, and J. Catto (2014), The relationship between clouds and dynamics in Southern Hemisphere extratropical cyclones in the real world and a climate model, *J. Geophys. Res. Atmos.*, *119*, 6609–6628, doi:10.1002/2013JD020699.

Received 5 AUG 2013
Accepted 23 MAY 2014
Accepted article online 28 MAY 2014
Published online 13 JUN 2014

The relationship between clouds and dynamics in Southern Hemisphere extratropical cyclones in the real world and a climate model

Pallavi D. Govekar[1], Christian Jakob[1], and Jennifer Catto[2]

[1] ARC Centre of Excellence for Climate System Science, Monash University, Clayton, Victoria, Australia, [2] School of Geography and Environmental Sciences, Monash University, Clayton, Victoria, Australia

Abstract The representation of clouds over the Southern Ocean in contemporary climate models remains a major challenge. A major dynamical influence on the structure of clouds is the passage of extratropical cyclones. They exert significant dynamical influences on the clouds in the dynamically active frontal regions as well as in the dynamically suppressed regions ahead and behind the cyclones. A cyclone compositing methodology is applied to a reanalysis and vertical profiles of cloudiness from CloudSat/CALIPSO to quantify the relationship between clouds and dynamics in extratropical cyclones over the Southern Ocean. It is found that the range of cloud fraction, vertical motion, and relative humidity changes considerably with height. There is a strong quasi-linear relationship between the three variables which changes with altitude. After establishing the observed relationships, the methodology is applied to the Australian Community Climate and Earth System Simulator to evaluate the model's ability to simulate the identified cloud-dynamics relationships. While the model is able to qualitatively reproduce the overall cloud structure, the circulation around the cyclone is generally too weak. As a result, the model fails to represent the observed cloud to dynamics relationship. This wrong relationship in the model leads to a misrepresentation of the cloud field manifested as either an error in the cloud fraction or as simulating the "right" clouds for the "wrong" reason. The result underscores the importance of relationship-oriented model evaluation techniques over simple right or wrong assessments.

1. Introduction

The simulation of clouds and their associated effects on the Earth's energy and water budgets in climate models remains a major challenge. Climate feedback associated with clouds is still a major source of uncertainty in the simulation of current and future climate [*Cess et al.*, 1990; *Bony et al.*, 2006; *Sanderson et al.*, 2008; *Lauer et al.*, 2010; *Zhou et al.*, 2013]. One reason for this challenge is the need to represent clouds by means of parametrization, as processes within them occur on scales much smaller than the climate model grid boxes. Successful parametrization of clouds requires the exploitation of relationship between resolved dynamical and thermodynamic variables and the macrophysical and microphysical cloud state. It is therefore important to evaluate how well current climate models capture the "dynamics-cloud" relationships.

Many recent studies have examined the representation of aspects of extratropical cloudiness as well as the radiation budget in climate models [*Klein and Jakob*, 1999; *Naud et al.*, 2010; *Field et al.*, 2011; *Bodas-Salcedo et al.*, 2012; *Williams et al.*, 2013; *Booth et al.*, 2013]. These studies have shown that most global climate models (GCMs) produce too small a radiative effect from clouds in the extratropics. Over the Southern Ocean these errors are particularly large and are consistent with an overestimation of absorbed solar radiation in the region [*Trenberth and Fasullo*, 2010].

The large biases over the Southern Ocean may be associated with sea surface temperature (SST) biases [*SenGupta et al.*, 2009], jet latitude biases [*Ceppi et al.*, 2012], and the well-known GCM double-Intertropical Convergence Zone problem [*Frierson and Hwang*, 2012; *Hwang and Frierson*, 2013]. Clouds have a profound influence in the Southern Ocean region, as the background albedo is low, leading to a large sensitivity of the radiative fluxes to the presence of clouds [*Cess et al.*, 1990; *Tsushima et al.*, 2006]. Storm tracks and their related extratropical cyclones and fronts are pronounced features of the Southern Hemisphere [*Trenberth*, 1991; *Simmonds and Keay*, 2000; *Berry et al.*, 2011]. Extratropical cyclones strongly affect the midlatitude distribution of cloud, precipitation, and water vapor. Clouds associated with these extratropical systems form

a substantial part of the total cloud field of the Southern Hemisphere [*Haynes et al.*, 2011]. It is conceivable that the cloud fields associated with these extratropical cyclones are connected to the large radiation errors in contemporary climate models making them a natural target for further study [*Field et al.*, 2011; *Bodas-Salcedo et al.*, 2012].

Satellite imagery, weather radar, and surface observations are all invaluable tools for the analysis of the mesoscale structure of cloud, precipitation, and winds related to cyclones. Analyses of extratropical cyclones using these tools have often been performed through case studies [*Neiman et al.*, 1993; *Browning and Roberts*, 1994; *Posselt et al.*, 2008]. Such case studies have contributed to the development of three-dimensional conceptual models that provide a foundation to understanding the dynamical evolution of cyclones. However, case studies have limitations as it is difficult to generalize their findings. Furthermore, case studies cannot easily be used to evaluate climate models as these models do not simulate an observed individual real-world cyclone. It is possible to force regional models with the large-scale fields from reanalysis products in order to examine case studies in the model; however, this does not allow a global analysis and does not provide information on the larger-scale influence of the model biases.

An alternative approach which enables information from a number of cyclones to be combined in a convenient form is to use a compositing technique. The compositing approach provides a useful way to remove cyclone-to-cyclone variability from both observational and model cyclones. Using compositing methods, several recent studies analyzed the cloud structure related to cyclones in observations [*Lau and Crane*, 1995; *Field and Wood*, 2007; *Govekar et al.*, 2011; *Naud et al.*, 2012] and models [*Klein and Jakob*, 1999; *Field et al.*, 2008; *Naud et al.*, 2010; *Field et al.*, 2011; *Bodas-Salcedo et al.*, 2012; *Booth et al.*, 2013].

Cloud processes are strongly influenced by dynamical processes at various scales. In the context of extratropical cyclones it is important for climate models to represent the large-scale dynamical processes and air flows around these systems in order to be able to correctly predict the clouds. If dynamical processes are poorly represented in the model, then there is no a priori reason to believe that the model can produce cloud fields with the right properties in the correct locations. Some studies focused on the dynamics of cyclones [*Norris and Iacobellis*, 2005; *Chang and Song*, 2006; *Catto et al.*, 2010; *Rudeva and Gulev*, 2011]. In this study we will directly link the three-dimensional distribution of clouds with the dynamics of a composite cyclone and quantify the relationships between them.

To improve the representation of Southern Hemisphere clouds in climate models, we need to first correctly identify the type, horizontal and vertical distribution, radiative effects, and organization of Southern Ocean clouds. Satellite data used in previous studies mostly relied on passive instruments thereby providing a quasi-two dimensional picture of the cloud field [*Lau and Crane*, 1997; *Klein and Jakob*, 1999; *Norris and Weaver*, 2001; *Webb et al.*, 2001]. Linking cloud with dynamics and quantifying their relationship based on such limited information is difficult. The more recently available active sensors on the CloudSat/CALIPSO [*Stephens et al.*, 2002] satellites provide cloud observations with high vertical resolution, albeit with very small footprints. This, for the first time, enables the construction of a fully three-dimensional picture of a composite extratropical cyclone from observations, which enables us to link clouds with dynamics and quantify the relationship between them.

Govekar et al. [2011] composited ≈ 800 cyclones to construct an estimate of the three-dimensional cloud and dynamical structure of Southern Hemisphere extratropical cyclones using CloudSat/CALIPSO observations and reanalysis data. Here we expand this analysis by compositing ≈ 3000 cyclones over a 2 year period and by quantifying the relationship between the dynamical fields and clouds in the composite cyclone.

The methodology developed in this study is then applied to a state-of-the-art climate model, the Australian Community Climate and Earth System Simulator (ACCESS) model. This allows us to not only evaluate the model's ability to simulate the concurrent cloud and dynamical structures related to cyclones but also to evaluate if the cloud and dynamical variables are related correctly to each other.

The structure of the paper is as follows. Section 2 describes the compositing techniques including how the CloudSat/CALIPSO data are to be compared to the model output, methodology, and ACCESS model. Section 3 discusses the observed composite cyclone's structure with a focus on the relationships between observed cloud and dynamical and thermodynamical variables. The ACCESS model is evaluated against observations in section 4. Section 5 discusses results, and conclusions are drawn in section 6.

2. Methodology and Data

2.1. The Cyclone Compositing Method

A cyclone compositing method that combines many individual cyclones into a composite cyclone is used here to determine the main characteristics of cyclones in the observations and in the model. The compositing technique is similar to that of *Govekar et al.* [2011]. The cyclones are identified and tracked using the Modeling, Analysis, and Prediction Climatology of Midlatitude Storminess method [*Bauer and DelGenio*, 2006]. We find the points along each cyclone track where the cyclone is in the 40°S–50°S latitudinal band and then draw a 4000 km × 4000 km grid box around each identified cyclone center. A new coordinate system, with 100 km grid spacing, is defined with the cyclone center as its central point ($x = 0$, $y = 0$), and all the cyclones are overlaid in that new cyclone-relative coordinate system. No attempt is made to link the identified cyclones in time, which means that individual cyclones at different times in their life are identified as separate data points in the composite. Of the 3163 cyclones found in the 2 year period of 2007/2008, 2038 have CloudSat/CALIPSO orbits intersecting them in the 6 h period. These were used to form the composite of the cloud structure shown here. We note that our experience shows that the minimum number of cyclones required to composite the active sensor data is 500. Hence, the results have converged to a robust average.

Note that, as shown in *Govekar et al.* [2011], we do not need to rotate cyclones according to their direction of propagation, owing to the well-organized front structure around the composite cyclone center (see also section 3). Mean sea level pressure (MSLP), vertical motion, and relative humidity from the National Centers for Environmental Prediction (NCEP)-Department of Energy (DOE) Reanalysis were composited using the above method to analyze the dynamical properties of the cyclone. These data were available to us at 2.5° × 2.5° horizontal resolution and on 17 pressure levels. The reanalysis data for all points within 2000 km of the cyclone center are included in the composite only when the CloudSat/CALIPSO data are available. The nearest NCEP-DOE level is assigned to the CloudSat/CALIPSO levels used in our analysis.

2.2. Compositing CloudSat/CALIPSO Data

CloudSat and the lidar satellite Cloud-Aerosol Lidar and Infrared Pathfinder Satellite Observation (CALIPSO) [*Winker et al.*, 2007] are part of the Afternoon A-Train [*Stephens et al.*, 2002] satellite constellation which provides global observations of clouds made by both active and passive sensors.The cloud profile radar (CPR) on board CloudSat is the first spaceborne radar with a wavelength (3 mm) that observes clouds vertically on a near-global scale. It measures the vertical structure of both cloud and precipitation from a Sun-synchronous orbit approximately 705 km above the Earth's surface. However, clouds with a small backscatter cross section, for example, optically thin cirrus with bases above 14 km, or low-level liquid cloud with small liquid droplets [*Marchand et al.*, 2008], are too tenuous to be observed by the CPR. Moreover, the CPR has a limitation in detecting boundary layer clouds whose presence is made ambiguous by noise associated with strong scattering of the Earth's surface. The cloud-aerosol lidar with orthogonal polarization (CALIOP) on the CALIPSO satellite fills in many of these gaps. It operates at shorter wavelengths (532 nm and 1064 nm) and is able to detect much smaller cloud particles. It also does not suffer from the surface contamination effect [*Mace*, 2010; *Haynes et al.*, 2011]. Details regarding the CPR and CALIOP instruments and the resulting data products can be found online (at http://cloudsat.atmos.colostate.edu).

To exploit the strength of both instruments in this study, we use the radar-lidar combined data from the 2B GEOPROF-LIDAR product to define a cloud mask at 240 m vertical and 1.4 km horizontal resolution. *Mace et al.* [2009] showed that the combination of CPR and CALIOP data is capable of detecting cloud occurrence, correctly identifying more than 90% of cloud layers as a cloud. If the CloudSat radar indicates the existence of a cloud (i.e., a cloud mask value of 20 or higher) or the CALIOP lidar indicates that the radar bin in question contains 50% or greater cloud cover then cloud is considered to be present. CloudSat cannot detect hydrometeors in the first kilometer above the surface [*Marchand et al.*, 2008]. The cloud data in the first kilometer are therefore discarded in this study.

The compositing method described in section 2.1 is adapted to composite the relatively sparse CloudSat/CALIPSO data. First, for each of the cyclones in the composite, the CloudSat/CALIPSO orbits that intersect the 4000 km × 4000 km cyclone area box are found. The cyclone area box is subdivided into 100 km × 100 km boxes, and the 2B-GEOPROF-LIDAR pixels are assigned to the appropriate box for each cyclone. Finally, the cloudy and total pixels falling into each box are counted to obtain the cloud fraction in each 240 m height bin around the composite cyclone. Following this method, the relatively sparse sampling

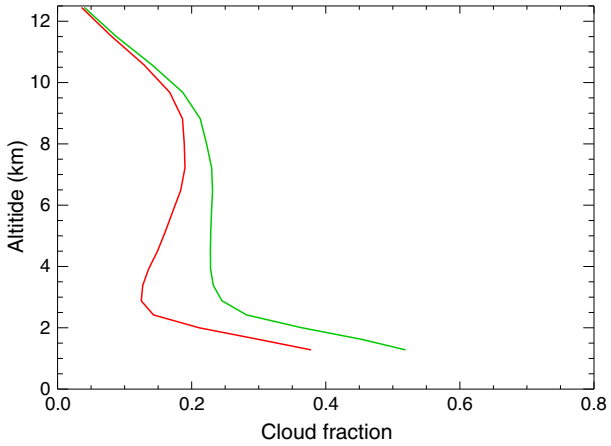

Figure 1. Cloud fraction as a function of height averaged over the 4000 km × 4000 km grid box around the cyclone center. The green line denotes the total cloud fraction from CloudSat/CALIPSO (upper bound), while the red line denotes cloud fraction only when there was no precipitation detected at the ground (lower bound).

of CloudSat is turned into a revealing composite cloud structure around the cyclone center [*Govekar et al.*, 2011].

To compare model simulations to the observed three-dimensional cloud and dynamical cyclone structure requires to match the model output with appropriate observations. There are two ways of doing this: (i) the use of an observation simulator and (ii) to retrieve the relevant model quantities from the observations. The Cloud Feedback Model Intercomparison Project Observation Simulator Package (COSP) [*Bodas-Salcedo et al.*, 2011] is a software tool that allows simulation of CloudSat data from models that is consistent with the model microphysics [*Field et al.*, 2011; *Bodas-Salcedo et al.*, 2012]. The COSP simulator was not available to us in the ACCESS model. It is worth noting, that even if it was, deriving products similar to the 2B-GEOPROF-LIDAR is not straightforward [*Mace et al.*, 2009]. Instead we follow the approach of *Jiang et al.* [2012] in processing the CloudSat/CALIPSO data for the evaluation of the model. There are several issues to consider. First, the model levels are not equally distributed and do not match the CloudSat/CALIPSO levels being denser at lower levels than at higher levels. To better match the observations, CloudSat/CALIPSO observations are averaged to match the model levels. As a result, at 1.6 km, 4.5 km, and 9.7 km, the model output is compared with the average of two, three, and four CloudSat levels, respectively. We find that the main cloud structures are preserved in the averaging (not shown).

A second issue for the comparison is that the CloudSat/CALIPSO data set includes precipitation in the cloud mask [*Haynes et al.*, 2009], and consequently, the estimated cloud fractions include a contribution from precipitation and are likely overestimated. *Haynes et al.* [2009] showed that inclusion of precipitation affects ≈12% of columns in the extratropical oceans. Following *Jiang et al.* [2012] we construct a second cloud mask (noprecip) by removing all cloud profiles for which precipitation was detected at the ground. The precipitation flags (rain, snow, drizzle, and graupel) in the CloudSat 2C-PRECIP-COLUMN product [*Haynes et al.*, 2009] are used to detect precipitation at the ground. Note that the original product can be considered an upper bound of cloud fraction as it counts precipitation as clouds and therefore will overestimate their fraction. On the other hand, the "noprecip" estimate constitutes a lower bound as it will only consider clouds with no precipitation at the surface. Since we remove the cloud fraction from the whole vertical column, there will be occasions where clear regions above the clouds will also be removed. This will reduce the difference between the two bounds at upper levels. However, these two bounds provide a rough estimate of uncertainty from the inclusion of precipitation in the cloud fraction estimate at precipitating points, which we consider the first-order problem in the data set. Note that these estimates do not address other issues of cloud detection, such as the misinterpretation of aerosol layers as clouds. As the latter are much smaller than the precipitation issue, we assess the model performance as poor if the model results lie outside our two observational estimates.

The cyclone data are available every 6 h, and we use all cyclones with centers in the 40°S–50°S latitudinal band in our analysis. We assign CloudSat/CALIPSO orbits to a cyclone if they cross the identified cyclone area ±3 h from the cyclone time. Figure 1 shows the vertical profile of cloud fraction averaged over the 4000 km × 4000 km cyclone composite box for the upper and lower bounds of the observations. The green line denotes cloud fraction for the upper bound of the observations while, the red line denotes the cloud fraction for the lower bound. In both cases, cloud fraction peaks at low levels consistent with the ubiquitous cloudiness at low levels in the Southern Ocean [*Haynes et al.*, 2011; *Govekar et al.*, 2011]. For the upper bound of the observations, the cloud fraction decreases from 0.54 to 0.22 between 1 and 3 km and then remains fairly constant between 3 and 9 km, above which it decreases to zero above 12 km. For the lower bound of the observations, the cloud fraction is smaller at all heights and it peaks up to 0.35 at low levels.

The difference between the values of cloud fraction at different heights indicates the presence of a multilayer cloud and precipitation structure in extratropical cyclones. As one might expect, the difference between the two observational estimates is largest at low levels, particularly below 3 km, where a significant amount of precipitation is present.

A final point worth noting is that as a result of the A-Train orbit the CloudSat/CALIPSO data is only available twice a day and therefore does not sample the full diurnal cycle. However, as our study focuses on points within the strongly dynamically active environment of an extratropical cyclone and as most of the systems in our sample have all their grid points located over the ocean we believe diurnal cycle effects on our results to be small.

2.3. The ACCESS Model

The global model used in this study is the atmospheric component of the Australian Community Climate and Earth System Simulator (ACCESS). The particular version used is based on the UK Meteorological Office atmospheric model (MetUM V7.1) and is based on the second version of the Hadley Centre Global Environment Model (HADGEM2-A) described in *Collins et al.* [2008]. We run the model in atmosphere only mode forced with observed sea surface temperatures (SSTs) using the Atmospheric Model Intercomparison Project experimental protocol. The model has a horizontal resolution of 1.875° longitude × 1.25° latitude (N96) and 38 vertical levels.

In contrast to the standard HADGEM2-A setup, the cloud scheme used in our simulations was the PC2 scheme (prognostic cloud and prognostic condensate [*Wilson et al.*, 2008]). This scheme carries prognostic variables for cloud fraction and cloud condensate (ice and liquid separately). Each physical process in the model, such as convection, turbulence, and large-scale motion, contributes to cloud formation and dissipation through individual source and sink terms. For more details on the cloud scheme formulation see *Wilson et al.* [2008]. The variable provided by the cloud scheme used here is the bulk cloud fraction. It represents the volume of a grid box covered by cloudy air (whether it is in liquid or ice phase). Other model variables used are vertical velocity, relative humidity, and MSLP. The temporal resolution of all the model output is 6 h.

As for the observed cyclones we use 2 years of model simulations to compare with CloudSat/CALIPSO observations. No significant differences in the location and frequency of occurrence of cyclones in the reanalysis and in the ACCESS model were found. We extract the bulk cloud fraction field from the model without using any simulator. The model cyclones are tracked using the method of *Bauer and DelGenio* [2006] applied to the MSLP field of the model. We find 3367 cyclones in the 40°S–50°S latitudinal band. Using the compositing method described in sections 2.1 and 2.2, model fields for MSLP, vertical motion, relative humidity, and cloud fraction related to tracked cyclones were composited and analyzed.

3. The Observed Composite Cyclone Structure

3.1. The Three-Dimensional Cloud and Dynamical Structure of the Composite Cyclone

We begin our analysis of the observed cloud-dynamics relationships by expanding the analysis of *Govekar et al.* [2011] to (i) include a much larger number of cyclones (≈2000) in the compositing and (ii) provide two observational estimates of the cloud structure. This analysis will form the foundation for the model evaluation carried out in the next section. Cloud fraction, MSLP, vertical motion,and relative humidity are composited at all heights, and some selected examples are shown in Figure 2. For orientation, we overlay the positions of cold and warm fronts identified at 850 hPa using the algorithm of *Berry et al.* [2011] as thick blue and red lines, respectively, in Figures 2a and 2d. The cloud fraction from the observations obtained with no filtering is shown at three heights in Figures 2a–2c. Figures 2d–2f show the cloud fraction at the same heights, if columns with precipitation at the surface are removed from the analysis. The difference between the two estimates is shown in Figures 2g–2i.

Figure 2a shows the mean cloud fraction at a height of 1.6 km together with the composite MSLP. The center of the composite cyclone with its average minimum pressure of ≈990 hPa is clearly identifiable. The low-level cloud maximum is well aligned with the pressure structure with a NW-SE tilt extending to the western side of the cold frontal region. Low clouds are also prevalent to the southern side of the cyclone center. Compared to the other two heights, the highest cloud fractions are found at this lowest altitude, consistent with findings of previous studies [*Mace et al.*, 2009; *Haynes et al.*, 2011; *Govekar et al.*, 2011]. Figure 2g shows that the difference between the upper and lower bounds of the observations is large near the center of the composite cyclone, consistent with the coexistence of low clouds and precipitation in that region.

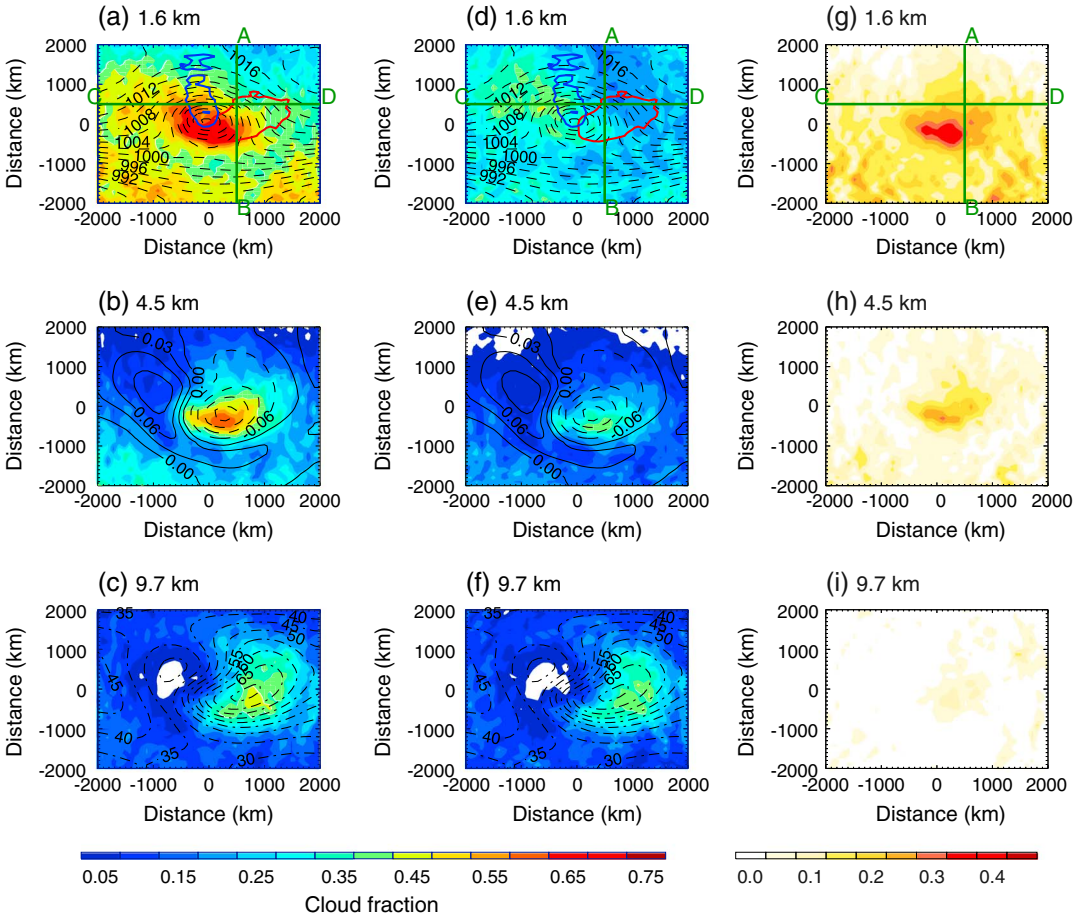

Figure 2. (a, d, and g) Cloud fraction and MSLP (hPa, dashed lines) at height 1.6 km, (b, e, and h) cloud fraction and vertical motion (Pa/s, solid line for downward motion and dashed line for upward motion) at 4.5 km, and (c, f, and i) cloud fraction and relative humidity (%, dash-dotted line) at 9.7 km. Figures 2a–2c show the observed total cloud fraction with no filtering for precipitation (upper bound), Figures 2d–2f show cloud fraction including only measurements when there was no precipitation detected at the ground (lower bound), and Figures 2g–2i show the difference between the two observational estimates.

Compared to the other two levels, the differences between the two cloud fraction estimates are largest at this height.

At 4.5 km (Figures 2b, 2e, and 2h), the maximum of cloud fraction is found in the warm frontal region. The superposed field in these panels is vertical motion which shows a strong dipole structure. Ascending regions (negative vertical motion, dashed) occupy the northeast quadrant of the system with strong descent (positive vertical motion, solid) found in the northwest sector and in an elongated band wrapping around the composite cyclone to the south. The cloud field follows a distinct "comma"-shaped structure similar to the vertical motion field. Overall, the vertical motion field is consistent with the findings of *Bauer and DelGenio* [2006, Figure 10]. However, there are some differences in the exact structure and magnitudes of the vertical velocities. This is not likely to be due to any differences between the Northern and Southern Hemispheres [*Naud et al.*, 2012], but may be due to their inclusion of only winter cyclones, and our composite including all seasons. The region of descent is a largely cloud free region at this level. The difference between the two observational estimates is largest in the warm frontal region, as expected by the surface rainfall characteristics (not shown).

At 9.7 km (Figures 2c, 2f, and 2i), the maximum cloud fraction moves to the eastern side of the cyclone center. The superposed field here is relative humidity (with respect to liquid water, %). The maximum of relative humidity and the maximum of cloud fraction are well aligned. At the leading edge of the warm frontal

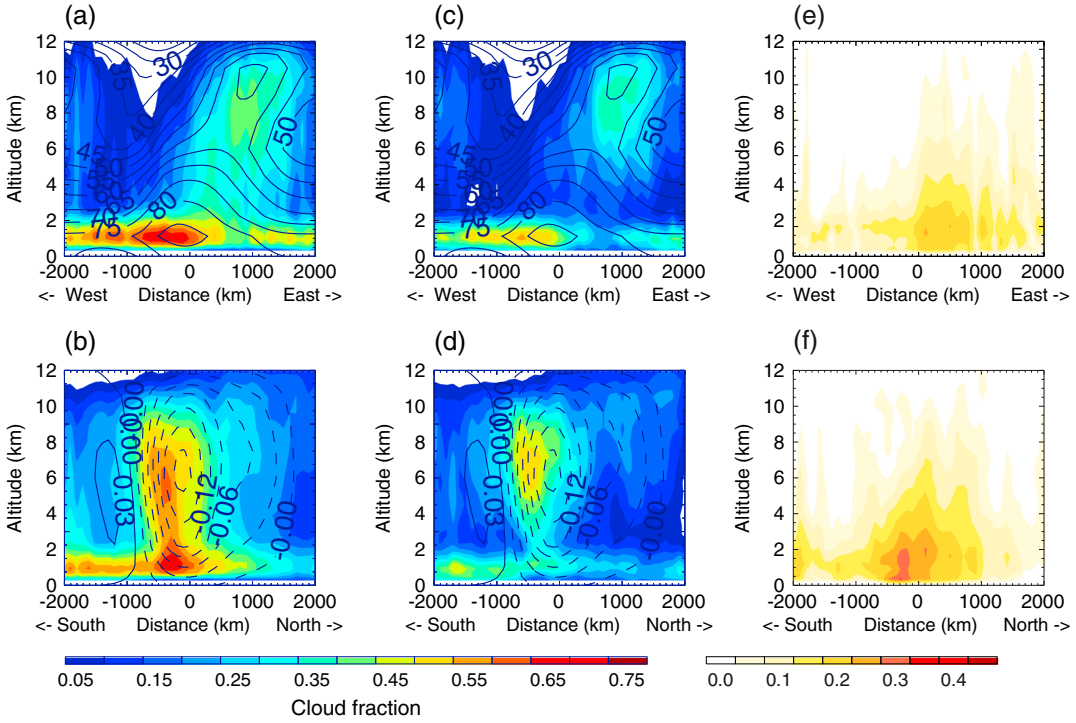

Figure 3. Cross sections of cloud fraction along the lines CD and AB in Figure 2. (a) Upper bound of cloud observation and relative humidity (RH) (%) at line CD. (b) Upper bound of cloud observation and ω (Pa/s) at line AB. (c) Lower bound of cloud observations and RH at line AB. (d) Lower bound of cloud observations and ω at line AB. (e and f) The difference between the two observational estimates at lines CD and AB, respectively. Dynamical fields are contoured and cloud fields are shaded.

region, thin cirrus clouds are evident. Our results agrees well with *Field and Wood* [2007] who showed that high-level cloud fraction related to extratropical cyclone exhibits a comma shape to the east of the cyclone center. The region behind the system is cloud free and dry. The difference between the observational estimates is small at this level. In the warm frontal region, high-level clouds are prevalent and their presence is independent of presence or absence of lower level clouds.

As we have quasi-continuous observations of cloud cover in the vertical direction, we can construct vertical slices of the cloud structure. Through these vertical sections, changes in the cloud field with height are easily identifiable. Two cross sections have been chosen: (i) an east-west cross section passing through both the cold and warm frontal regions (Line CD in Figure 2a) and (ii) a north-south section through the center of the warm frontal region (Line AB). Figure 3 shows the vertical cloud structure for those two cross sections overlaid with relative humidity (Figures 3a and 3c) and vertical motion (Figures 3b and 3d).

A tilted cloud structure is clearly visible in the section taken 500 km north of the cyclone center (Figures 3a and 3c). Relative humidity matches well with the cloud fraction with two maxima, one at the lower levels, at about 2 km, and another at high levels around 10 km. This is consistent with the large-scale ascent in the warm conveyor belt (also shown in the observational study of *Govekar et al.* [2011]). Figure 3b shows a north-south slice of the three-dimensional cloud structure together with ω taken at 500 km to the east of the center (along line AB). This cross section crosses the warm front region (see Figure 2). Most of the clouds occur in the region of ascent with two peaks, one at about 2 km and another at about 6 km. This result agrees with *Booth et al.* [2013] who showed that the spatial distribution of ω is consistent with the cloud fraction. There is also a slight tilt in the cloud field from north to south, consistent with the structure of clouds across warm fronts shown in *Naud et al.* [2010].

Taken together, the composite three-dimensional structure of clouds depicted in the Figures 2 and 3 resembles the classical conceptual models of extratropical cyclones [*Bjerknes and Solberg*, 1922]. The warm frontal region is characterized by thick high-top clouds, maximum ascent, and high relative humidity. In the cold

frontal region, thick clouds are found to the north side of the cyclone center. Midlevel cloud extends to the southeast of the cyclone center. Low-level clouds are dominant in the system and are present at various heights at the northwest side of the cyclone center, which is also a region of strong subsidence. Excluding CloudSat/CALIPSO observations that contain precipitation at the surface primarily reduces cloud fraction at low levels in and near the center of the composite cyclone and to the south of the cyclone. Given the large differences and the uncertainty in the observations combined with the absence of simulator information, we treat the two observational cloud fraction estimates as upper and lower bounds in the model evaluation carried out below.

3.2. The Observed Relationships Between Clouds and Dynamics

Cloud structures are invariably linked to the internal circulations that accompany the cyclone. We use the three-dimensional structure of clouds derived in the previous section to quantitatively relate it to the three-dimensional large-scale fields in the composite cyclone. We choose two large-scale variables that have been found to be important for the formation and dissipation of clouds and have often been used in cloud parametrization, namely, vertical motion and relative humidity [*Slingo*, 1997; *Wilson et al.*, 2008].

Figures 4a–4c show the relationship between cloud fraction, vertical motion, and relative humidity for the upper bound of cloud fraction at three different heights. The vertical motion is on the *x* axis, RH is on the *y* axis, and the color of the points denotes the value of cloud fraction. The slope of the regression line and the correlation coefficient (*R*) between omega and RH are shown on each panel. Note that the shape of the scatterplot will remain the same for the lower bound of the observations. This is because the observed vertical motion and relative humidity are identical.

We can see that at all levels, there is a relationship indicating higher relative humidity in regions of stronger ascent, consistent with adiabatic cooling in the ascent region. This linear relationship breaks down in the descent region. The magnitude of the slope is smaller (−72.97) at the lowest level and higher at the upper level (−170.79). This is associated with the proximity to the ocean surface at 1.6 km favoring large RH. As clouds in this region form largely through boundary layer turbulence, large-scale velocities will have a smaller impact on cloud fraction. It is worth noting that these relationships will be affected by the quality of the data set used. There are previous studies which show that NCEP-DOE performs well over the Southern Ocean, compared to other available reanalysis data sets. For example, *Betts et al.* [2006] compared NCEP-DOE data with ERA 40 and showed that the difference between relative humidity in the two data sets over the Southern Ocean is negligible (their Figures 4 and 5). However, these reanalysis data are derived using models and both could have errors over the Southern Ocean.

To understand whether the different dynamical regimes seen in the scatterplots correspond to particular regions of the composite cyclone, we have color coded the geographical location of these regimes according to the colored boxes overlaid on the scatterplots. The purple box contains the points from the composite cyclone where the highest relative humidity and the strongest ascent occur. The red box contains the points where the values of relative humidity and ascent are in the intermediate range. The light green box contains those points where the values of vertical motion are close to zero and relative humidity is low, and the dark green box contains points with the strongest descent and relatively low relative humidity.

The overall relationship indicates higher relative humidity in regions of stronger ascent, consistent with adiabatic cooling in the ascent region. However, the slope is more acute at higher altitudes than that at the lower altitudes. At 1.6 km (Figure 4a), the proximity to the ocean surface favors large RH. As clouds in this region will form largely through boundary layer turbulence, large-scale velocities will have a smaller impact on cloud fraction. Figure 4d shows that, as expected, the combination of these variables is not random in space but follows the dynamical structure of the composite cyclone. Points that exhibit the strongest ascent and highest relative humidity are located at the center and eastern sides of the cyclone and corresponds to highest values of the cloud fraction in the region (cf. Figure 2a). The points with slightly weaker ascent and lower relative humidity within the red box come from a region around the cyclone center corresponding to the large-scale uplift in the warm conveyor belt region, and at the S-W of the cyclone, the latter is influenced by another system in the wake of the main one (not shown). The region of descent is relatively dry and is at the western side of the cyclone center, behind the system corresponding to the "dry slot" and smaller values of cloud fraction (cf. Figure 2a). Points with small vertical motion and low relative humidity are found toward the outer edges of the composite cyclone again resulting in smaller values of cloud fraction in the region.

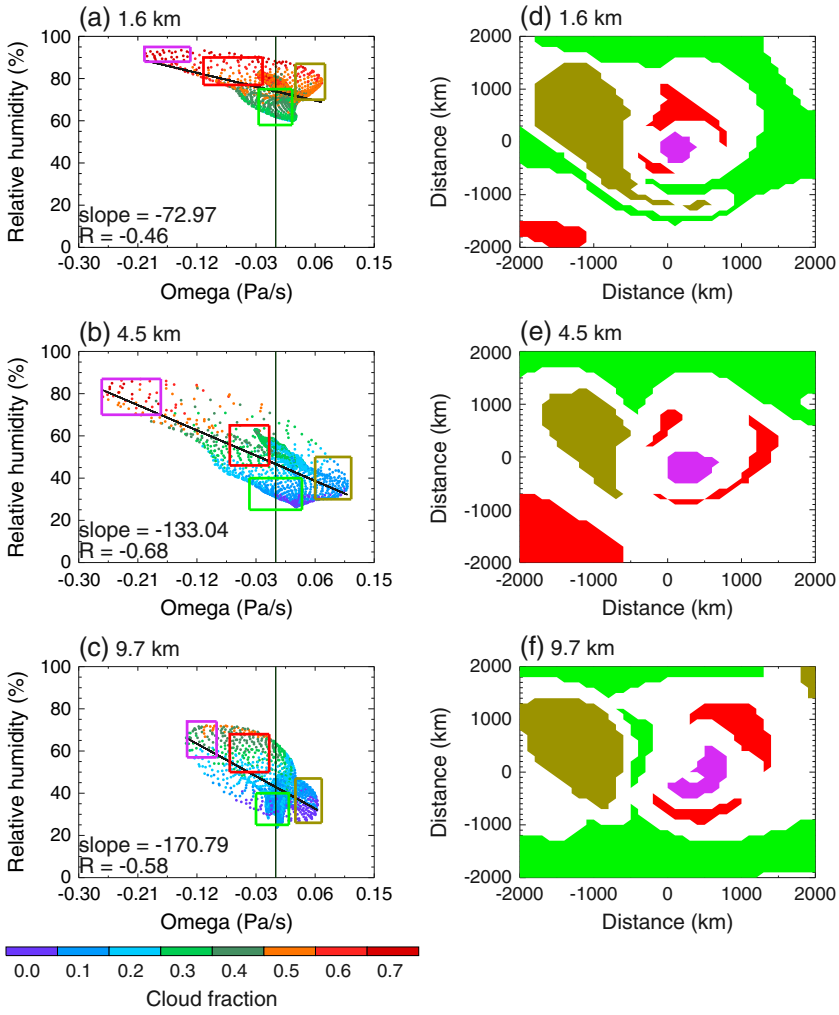

Figure 4. Cloud fraction in terms of vertical motion (Pa/s) and relative humidity (%) at height (a and d) 1.6 km, (b and e) 4.5 km, and (c and f) 9.7 km. Figures 4a–4c show results for all cloud observations. Figures 4d–4f show regions of particular interest in the scatterplot (see text for details). The color of the point denotes the value of cloud fraction.

Figure 4b shows that the cyclone's midlevels experience the widest range of relative humidity and vertical motion. Again, different regions in the scatterplots correspond to distinct locations in the composite cyclone (Figure 4e). Overall, the cloud fraction values are 50% smaller at this level than they are at the 1.6 km level, for given value of ω. The region of strong ascent is very moist, has high cloud fractions, and is situated at and to the east of the cyclone center. As at the 1.6 km level, this area is surrounded by a region of medium ascent, lower relative humidity, and quite small cloud fractions. At 9.7 km the range of vertical motion is the smallest of all three levels while there is still a wide variation of relative humidity (Figures 4c and 4f). While the scatter of points is broader at this level, there is still a strong relationship between relative humidity and vertical velocity. The boxes are taken from different regions on the scatterplot for each different heights due to the different distribution of points. These color-coded regions are shown in Figures 4d–4f.

To provide a different perspective on the cloud-dynamics relationships, Figure 5 shows scatter diagrams of cloud fraction versus relative humidity with vertical motion indicated by the color of the points. The figure shows upward and downward motion points separately to investigate if the relationship between cloud fraction and relative humidity changes with the sign of vertical motion. Figures 5a–5f show the results for subsiding motion ($\omega > 0$) and Figures 5g–5l those for ascending motion ($\omega < 0$). Table 1 shows linear regression coefficients for the relation between cloud fraction and relative humidity at the three levels. These figures all show a linear relationship between RH and cloud fraction, whether in an ascending or descending

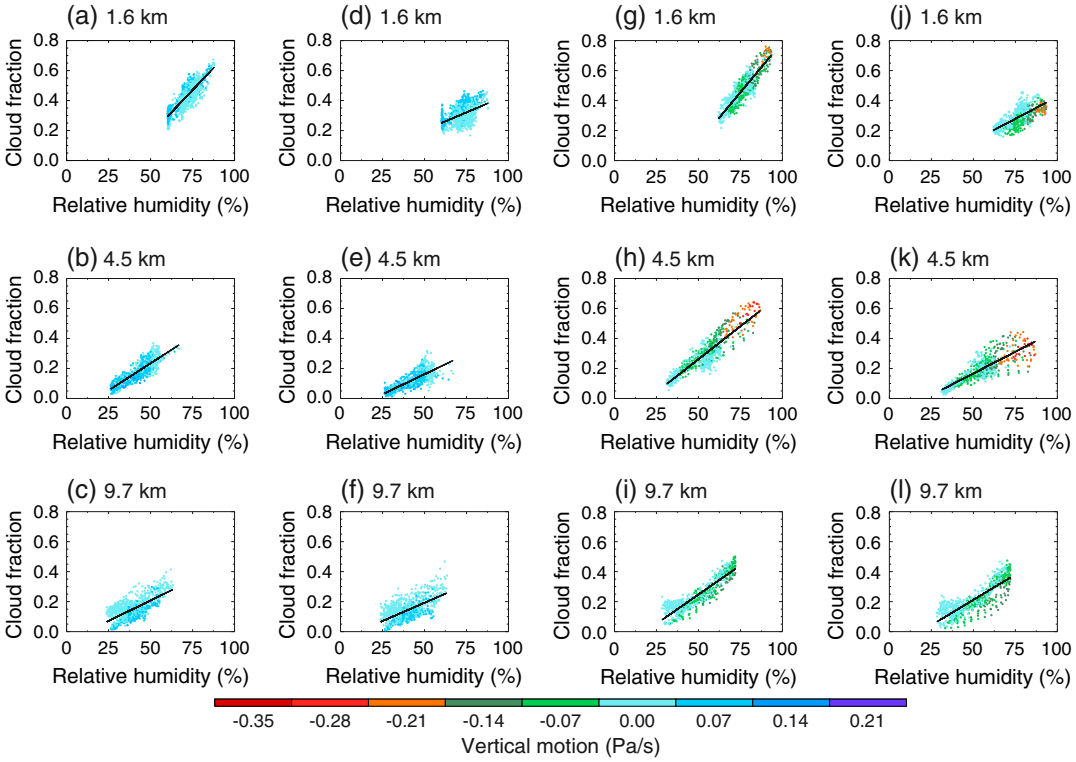

Figure 5. Vertical motion (Pa/s) in terms of the relative humidity (%) and cloud fraction for the two observational estimates in the (g–l) ascent and (a–f) descent region. Figures 5a–5c and 5g–5i show results for all cloud observations. Figures 5d–5f and 5j–5l show results for cloud observations with no precipitation at the surface. The color of the points denotes the value of vertical motion.

regime, consistent with the findings of *Naud et al.* [2010] (see their Table 2). This relationship is strongest at the lowest level with a slope of 0.0138 (Table 1) for the upper bound in the ascending regime. As expected from Figures 2 and 3, the removal of clouds with surface precipitation strongly affects the relationships at the lowest level (see also Table 1).

To complete the picture of the relationships between cloud fraction, relative humidity, and vertical motion, Figure 6 shows the relative humidity in terms of cloud fraction and ω. Considering first the upper observational bound, at all levels there is a linear relationship between ω and cloud fraction. This relationship is weakest at the lowest level (shown by the smallest slope and R value of only −0.36). When the contaminating precipitation is taken out of the observational estimate, the relationship weakens at all levels and is absent at the lowest level. This is consistent with strong ascent leading to precipitating cloud.

To summarize, cloud fraction is linearly dependent on relative humidity and it is dependent on vertical motion when precipitation is contaminating. All the relationships are weaker in the region of descent. It is worth noting that all relationships shown in the previous figures are representative for a highly averaged composite cyclone and they might not necessarily reflect the behavior of any individual cyclone.

4. The Composite Cyclone Structure in the Model

4.1. The Three-Dimensional Model Cloud Structure

Using the compositing method described in section 2.1, model fields for MSLP, vertical motion, relative humidity (with respect to water), and cloud fraction related to the tracked cyclones are composited and are shown in Figures 7 and 8. Figures 7a–7c show the model results. The difference between model and the upper bound of the observations is shown in Figures 7d–7f, and the difference with the lower bound is shown in Figures 7g–7i. While the model and the observations exhibit broadly similar cloud structures, there are several model deficiencies. As in the observations, at 1.6 km, the model exhibits large values of cloud fraction near and to the eastern side of the composite cyclone center. However, the model severely

Table 1. Linear Regression Coefficients for the Relation Between Cloud Fraction and Relative Humidity (%) at Three Levels in Observations and ACCESS Model as Shown in Figures 5 and 10

			Slope	Intercept	R	R^2
$\omega > 0$	Upper bound	1.6 km	0.0117	−0.41	0.83	0.69
		4.5 km	0.0072	−0.12	0.89	0.81
		9.7 km	0.0054	−0.65	0.69	0.48
	Lower bound	1.6 km	0.0047	−0.035	0.47	0.23
		4.5 km	0.0054	−0.11	0.83	0.70
		9.7 km	0.0048	−0.051	0.63	0.40
	Model	1.6 km	0.0086	−0.46	0.93	0.86
		4.5 km	0.0041	−0.09	0.91	0.82
		9.7 km	0.0078	−0.21	0.87	0.75
$\omega < 0$	Upper bound	1.6 km	0.0138	−0.58	0.89	0.80
		4.5 km	0.0088	−0.17	0.91	0.83
		9.7 km	0.0079	−0.15	0.48	0.84
	Lower bound	1.6 km	0.0060	−0.18	0.70	0.49
		4.5 km	0.0057	−0.11	0.84	0.70
		9.7 km	0.0070	−0.14	0.84	0.71
	Model	1.6 km	0.011	−0.65	0.77	0.60
		4.5 km	0.0071	−0.18	0.70	0.49
		9.7 km	0.014	−0.52	0.79	0.63

underestimates the widespread low cloud cover away from the cyclone center, especially in the strongly subsiding conditions in the N-W quadrant of the cyclone. *Bodas-Salcedo et al.* [2012] and *Williams et al.* [2013] found a negative shortwave radiation bias in this region of the cyclone. By analyzing a case study, *Williams et al.* [2013] suggested that the coarse vertical resolution of the model may contribute to these biases. Some recent studies have shown that GCM's have large biases in the shortwave cloud radiative effect (CRE), which is defined as difference between clear and full sky conditions, in the N-W part of the composite cyclone [*Field et al.*, 2011; *Bodas-Salcedo et al.*, 2012]. The lack of clouds at lower levels is consistent with that bias. The model has a minimum MSLP of 991 hPa, indicating that the model cyclone is not deep enough compared to the observed composite cyclone. This is consistent with *Bauer and DelGenio* [2006] who showed that GCM cyclones are shallower than those in the reanalysis.

At midlevels around 4.5 km, clouds can be seen in the eastern part of the composite model cyclone center in Figure 7b. The vertical motion shown in Figure 7b shows a dipole structure as in the observations (Figure 2b) with ascent at the eastern side of the cyclone center and sinking motion to the west of the cyclone center. However, the vertical motion in the model is weaker than observed. The ascent is ≈50% weaker and follows a comma-shaped structure with an exaggerated N-E tilt compared to the observations (Figures 7e and 7h). The descent is also too weak. Most of the clouds are in the region of ascent, and the region of descent is cloud free as it is in the observations. At this level the model values lie between the two observational estimates, making it difficult to judge the model performance. If at all the model slightly underestimates cloud fraction in the region of ascent (Figures 7e and 7h), with values close to the low observational estimate. Overall, the clouds at midlevels are much better simulated than those at low levels.

Figure 7c shows the cloud fraction and relative humidity from the model at 9.7 km. The maximum of the model cloud fraction is colocated with the maximum relative humidity. Clouds occur mainly in the eastern part of the cyclone, and there are few clouds behind the composite cyclone center, consistent with very dry air in the region. The model produces slightly higher cloud fractions than observed, in particular near the center of the composite cyclone. However, in the northeastern part of the cyclone, the model underestimates cloud fraction consistent with lower values of relative humidity than observed (Figures 7f and 7i). To the west of the cyclone center, the model has higher relative humidity than the observation, consistent with the weaker circulation identified at lower levels.

Figure 8 shows model cross sections of cloud cover taken 500 km north of the cyclone center and 500 km east (cf. Figure 3 for the observed clouds) of the cyclone center along with the model error calculated from the two observational estimates.

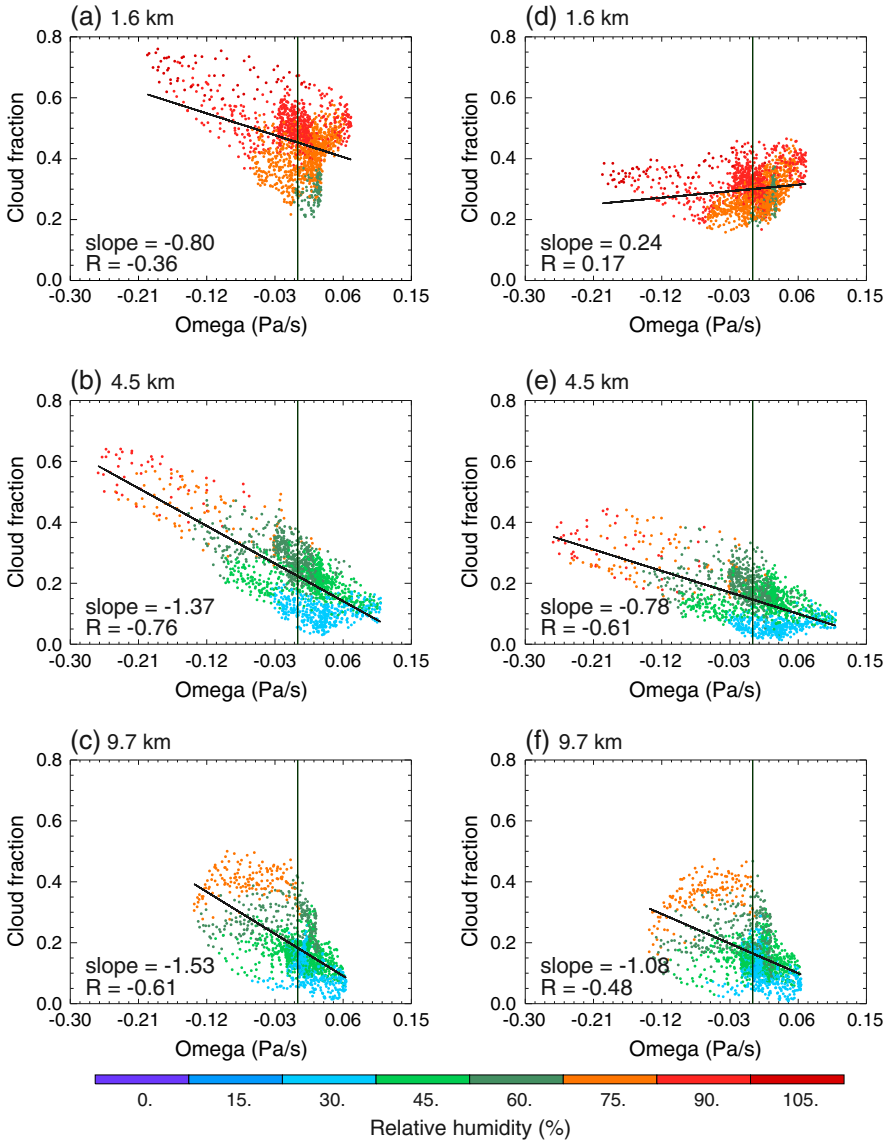

Figure 6. Relative humidity (%) in terms of the vertical motion (Pa/s) and cloud fraction for the two observational estimates at (a and d) 1.6 km, (b and e) 4.5 km, and (c and f) 9.7 km. Figures 6a–6c show results for all cloud observations. Figures 6d–6f show results for cloud observations with no precipitation at the surface. The color of the points denotes the value of relative humidity.

Figure 8a shows two maxima of cloud cover, one at low levels and another in the upper levels of the warm frontal region. Two maxima of relative humidity coexist with the cloud maxima. The upper troposphere behind the system is largely cloud free and dry. The model cloud fraction at low levels is severely underestimated compared to both sets of observations (Figures 8c and 8e). Hence, we are confident that this finding constitutes a real model error, rather than an artifact of the comparison method. The relative humidity at high levels in the model is underestimated in the eastern part of the cyclone and overestimated in the western part again hinting at a too weak ascent and descent in and behind the cyclone center.

Composite cloud fraction and vertical motion from the model at 500 km east of the cyclone center are shown in the Figure 8b. This cross section passes through the warm frontal region (indicated by the red contours in Figure 2). There is a maximum in cloud fraction just south of the center of the composite model cyclone which gradually extends farther south at higher levels. Clouds are underestimated in the model below 8 km, mainly to the south of the cyclone center. However, clouds above 9 km are overestimated

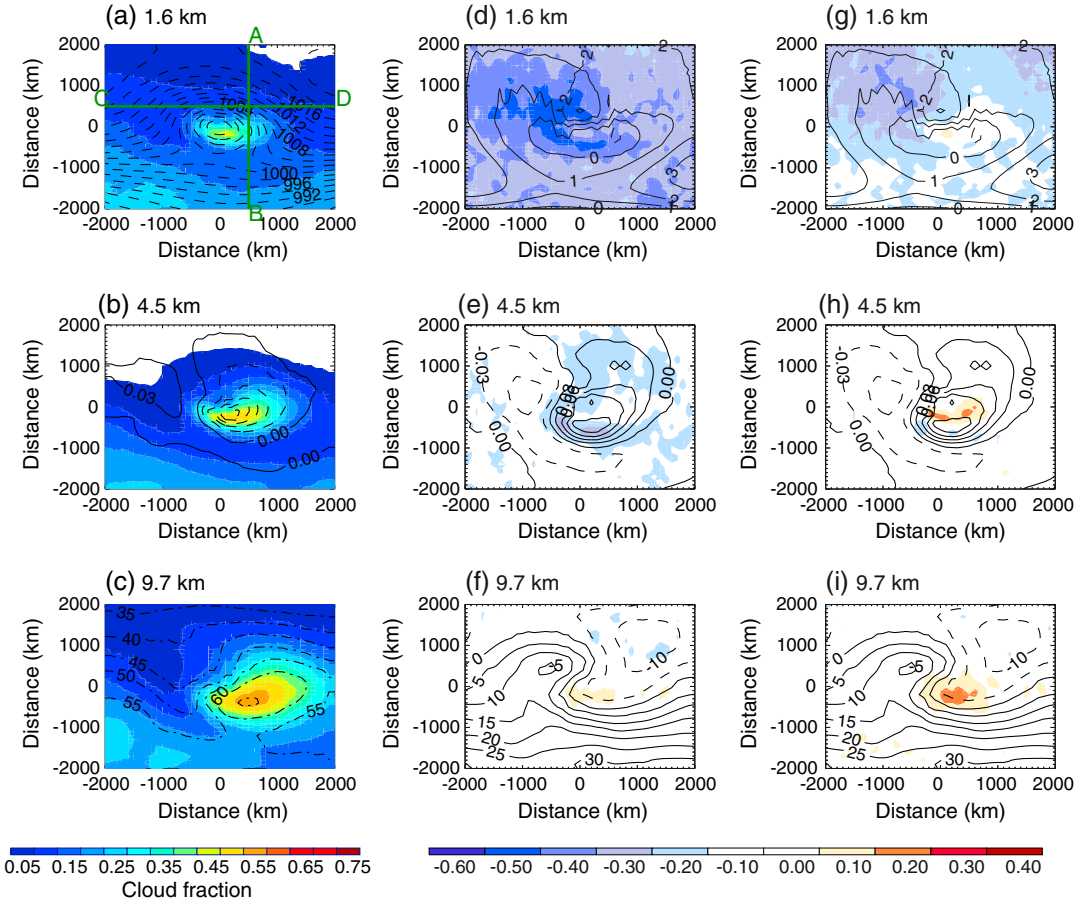

Figure 7. Model cloud fraction and differences with the observations at three different heights. (a) Model cloud fraction at 1.6 km and MSLP (hPa). (d) Difference between model cloud fraction and the upper bound observations along with the MSLP error. (g) Difference between model cloud fraction and the lower bound observations along with the MSLP error. (b) Model cloud fraction and ω (Pa/s) at 4.5 km. (e) Difference between model cloud fraction and the upper bound observations along with ω differences. (h) Difference between model cloud fraction and the lower bound observations along with ω differences. (c) Model cloud fraction and relative humidity (%) at 9.7 km. (f) Difference between model cloud fraction and the upper bound observations along with RH differences. (i) Difference between model cloud fraction and the lower bound observations along with RH differences. Dynamical fields are contoured and cloud fields are shaded.

in the model (Figures 8c and 8e). Most of the clouds are in the region of ascent. The region of descent is cloud free except at very low levels, where model cloud fraction is once again too low. As was already evident in Figure 7, the rising motion and the descending motion are too weak in the model throughout the entire troposphere.

4.2. The Relationships Between Clouds and Dynamics in the Model

After investigating the overall distribution of clouds and key dynamical fields in the model, we now study more closely how the clouds relate to the dynamics with the same method as for the observations. Figure 9 shows the relationship between vertical motion, relative humidity, and cloud fraction at three different heights in the model, just as Figure 4 did for the observations. The *x* axis denotes vertical motion and the *y* axis relative humidity. The color of the point denotes value of cloud fraction. As for the observations, the colored boxes drawn in Figure 9 denote areas of particular interest. Figures 9d, 9e, and 9f show the position of points in each colored box related to the (composite) cyclone center in the model. As the model does not reproduce the range of observed values, the boxes have been placed in regions that are qualitatively similar in the model to those in the observations shown in Figure 4.

Figure 9a shows cloud fraction–vertical motion–relative humidity relationship in the model at 1.6 km. It is evident that while the shape of the scatterplot from the model is similar to the observations, its variability

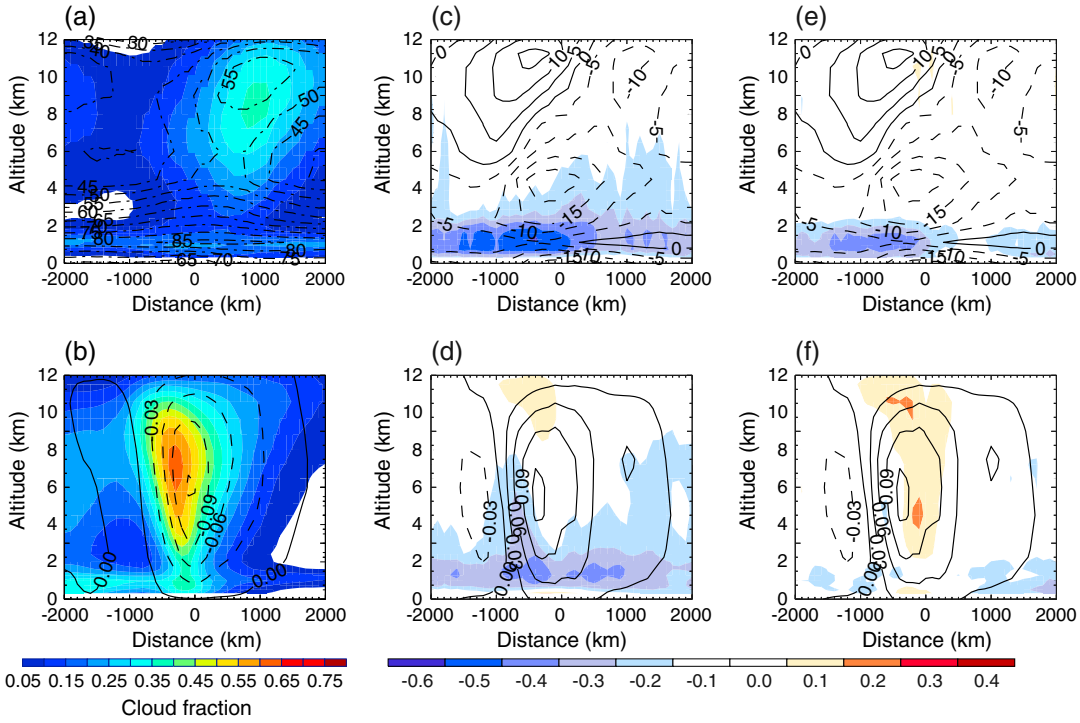

Figure 8. Cross section of cloud fraction along the lines CD and AB in Figure 7. (a) Model cloud fraction and RH (%) are shown at line CD and (b) model cloud fraction and ω(Pa/s) at line AB. Figures 8c and 8d show the difference between the model cloud fraction and RH and the upper bound observations. Figures 8e and 8f shows the difference between the model cloud fractions and RH and the lower bound observations. RH and ω are contoured, and cloud fields are shaded.

across vertical motion and relative humidity is much smaller (cf. Figure 4). However, the model captures the most basic relationships with higher relative humidity for stronger ascent and vice versa. The values of cloud fraction are very small in the model, consistent with the underestimation of low-level clouds shown in Figure 7. The maximum value for the ascent is −0.12 Pa/s, and the maximum value for relative humidity in the model is 80% compared to −0.24 Pa/s and 95% in the observations. Hence, the model clouds exist in much drier air than those in the observations. Some earlier studies found that it is humidity biases in models that are often responsible for lower level relative humidity biases [*Su et al.*, 2011]. The descent in the model is also weaker than in the observations. The region of descent with high values of relative humidity is essentially absent in the model. Clouds in the region of ascent also exist in lower than observed relative humidities and values of ascending motion.

At 4.5 km, the model values of relative humidity reach up to 65% and the model ascent values peak around −0.18 Pa/s (Figure 9b). The range of all variables is again too small compared to the observation. However, in relative terms the range of vertical motion and relative humidity at this midlevel is larger than at the other two levels shown and the relationship between vertical velocity and relative humidity is slightly stronger, consistent with the observations. The region of descent has weaker values than observed and clouds in this region are largely absent. This figure is consistent with the weak vertical motion field in the model, shown in Figure 7.

The values of model cloud fraction at the 9.7 km level (Figure 9c) are higher than those in the observation. This is despite the fact that the ascent in the model is more than 50% weaker than observed. The descent is again too weak compared to observations, and once again, the range of vertical motion and relative humidity are strongly underestimated.

The purple box includes the points where the highest relative humidity and highest ascent value are achieved in the model. These points are located near and to the east of the cyclone center consistent with the observations at all heights (cf. Figure 4). The red box includes points of medium ascent and middle-to-high values of relative humidity. These points surround the region with the highest ascent values and highest humidity values near the cyclone center in the model which is consistent with the observations.

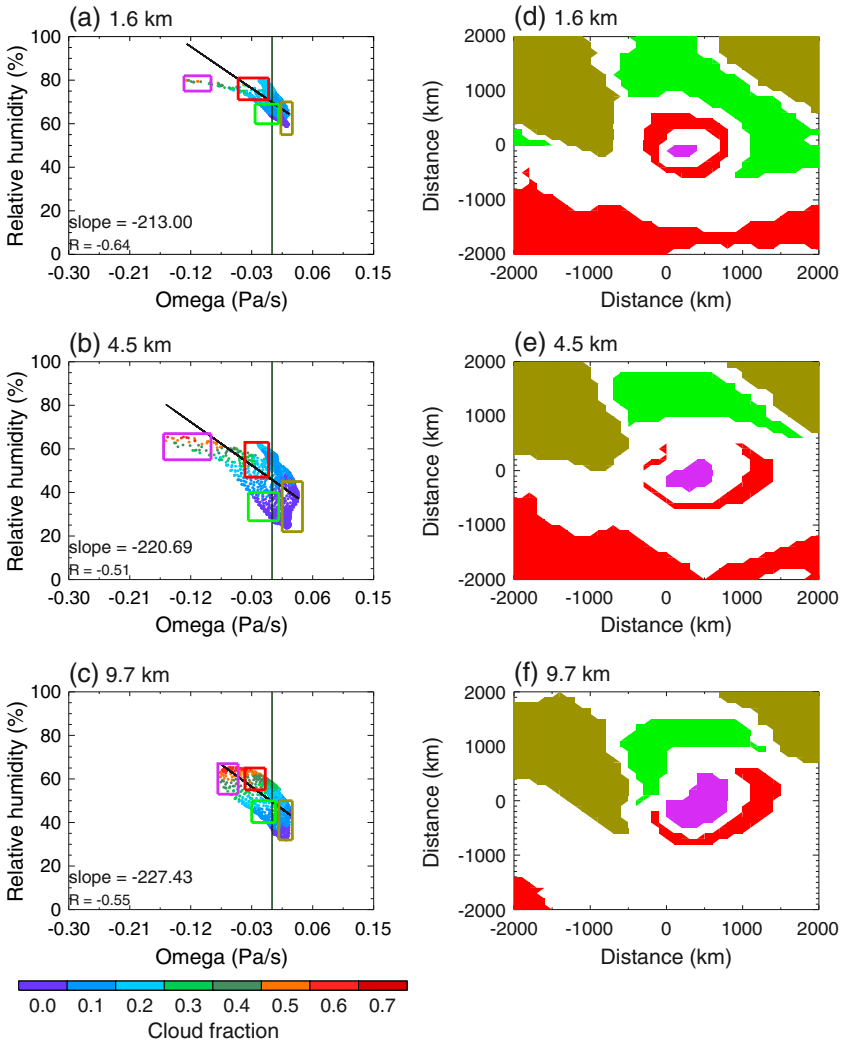

Figure 9. Cloud fraction in terms of the ω (Pa/s) and relative humidity (%) from the model at height (a and d) 1.6 km, (b and e) 4.5 km, and (c and f) 9.7 km. Figures 9a–9c show the model results. Figures 9d–9f show the regions of interest identified by colored boxes in the scatterplots. The color of the point denotes the value of cloud fraction. See Figure 4 for the observation equivalent.

Points with these characteristics can also be seen in the southwestern part of the domain in both model and observations. However, contrary to the observations, the model also produces these characteristics to the south of the cyclone, where the observations indicate drier conditions with weaker to no ascent. The points in the region of descent (dark green box) are relatively dry and can be found behind the system in both the model and observations. Unlike the observations, the model also produces points with strong descent and low values of relative humidity in the northeastern part of the cyclone. The remaining points have small vertical motion and are relatively dry. They are well represented in the northern half of the composite but are misrepresented in the southern half. In summary, Figure 9 illustrates that while in a relative sense the model represents the cyclone structure somewhat realistically, it does so with a severe underestimation of the absolute values of key variables and too small a variability across the composite.

Figure 10 shows vertical motion in terms of the relative humidity (%) and cloud fraction in the model. It is evident that the model does not show the same quasi-linear relationship between relative humidity and cloud fraction seen in the observations, especially at the highest and lowest levels (cf. Figure 5). Table 1 shows that the linear regression slopes from the model do lie in between the upper and lower bounds, but the shape of the scatterplots are quite different. In the weaker range of ascent relative humidity in the model

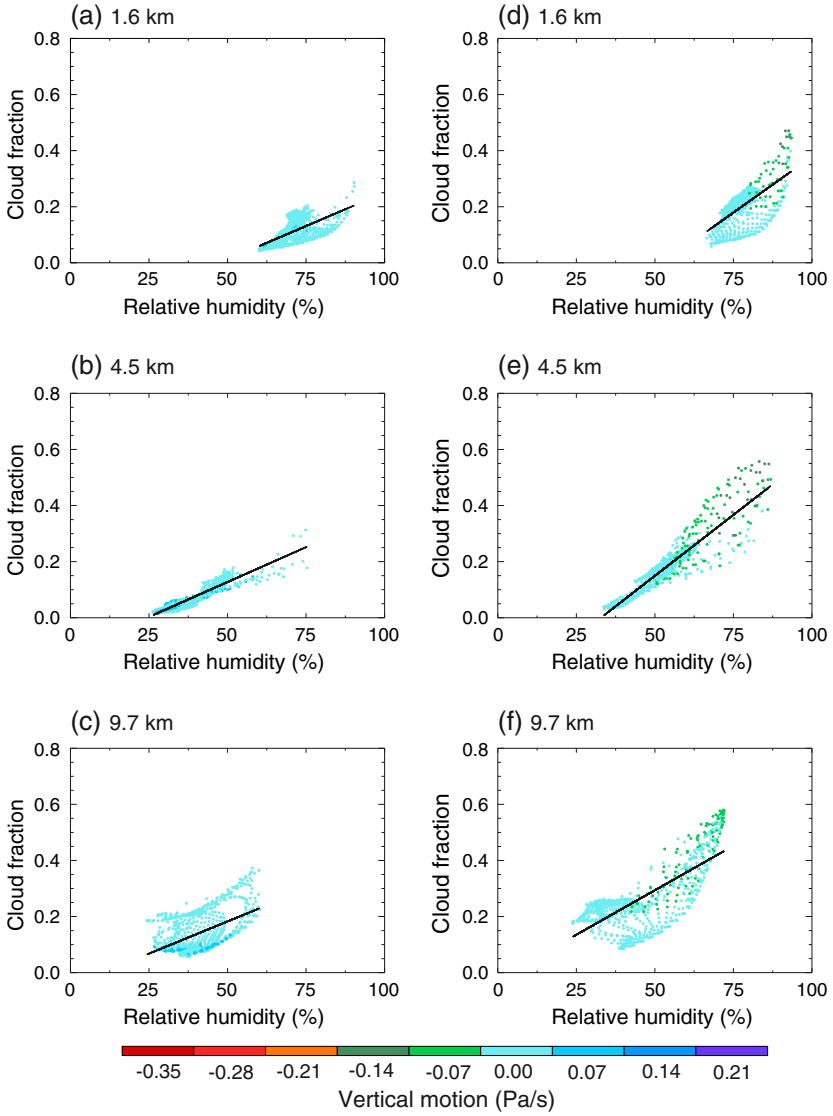

Figure 10. Vertical motion (Pa/s) in terms of the relative humidity (%) and cloud fraction from the model at (a) 1.6 km, (b) 4.5 km, and (c) 9.7 km height. The color of the points denotes the value of vertical motion.

is much greater than that observed while in the strong ascent regime, the model underestimates relative humidity (cf. Figures 4 and 9).

Figures 5 and 10 suggest that for a given relative humidity, cloud fraction in the model is larger than the observations (using the lower bound), unless relative humidity is very low. So even if the model could reproduce the right range of ascent/descent in the cyclones, this would not necessarily produce the right amount of clouds if the moisture structure remains unchanged in the model. Vertical motion in the model is too weak compared to the observations and the relationship between vertical motion and relative humidity, and cloud fraction and relative humidity are wrongly produced by the model.

Figure 11 shows the relative humidity in terms of vertical motion and cloud fraction in the model at three different heights. At 1.6 km, the points in the region of ascent have higher values of relative humidity. The region of descent is dry and shows lower values of cloud fraction. Compared to Figure 6, the range of large-scale variables is too small at all three heights. The shape of the scatterplots for all three heights is again very different in the model from that in the observations (cf. Figure 6). Furthermore, the values of slope and coefficient of regression noted on the panels of Figure 11 show that the steepness in the scatterplot increases with height in the model. For 1.6 km, the slope of the regression line is 2.85 which gradually

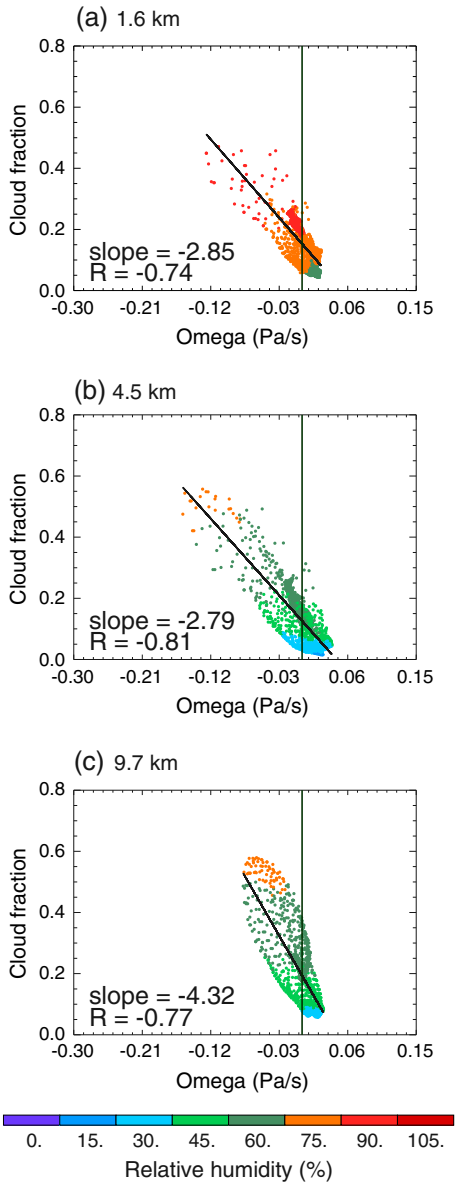

Figure 11. Relative humidity (%) in terms of the vertical motion (Pa/s) and cloud fraction from the model at (a) 1.6 km, (b) 4.5 km, and (c) 9.7 km height. The color of the points denotes the value of relative humidity.

increases with height and reaches a value of 4.3 at 9.7 km. However, in the observations, the steepness remains overall the same for all heights. In the model many points are located in a small region which is contradictory to observations where all the points are distributed over larger area (cf. Figure 6). The number of points with high values of relative humidity is larger at 9.7 km than that at 4.5 km which is consistent with highest values of cloud fraction found at the higher level (Figure 9).

In summary, we find that while the model produces an overall reasonable spatial cloud structure related to extratropical cyclones, the relationship between cloud fraction and the larger-scale variables is not correctly simulated. The range of dynamical variables in the composite cyclone is smaller than observed, indicating that the dynamical properties of the model cyclones are not well simulated. Consequently, even where clouds are simulated well in the model, it is unlikely that this is for the correct reason. A caveat to that conclusion is that the relationships investigated here are those in a highly averaged composite system and therefore do not reflect instantaneous behavior.

5. Discussion

The recently available CloudSat/CALIPSO data provide an opportunity to add a third dimension to the study of clouds in extratropical cyclones. These modern satellite data were used to construct a picture of the three-dimensional structure of clouds within Southern Hemisphere extratropical cyclones. Related dynamical fields from reanalysis were composited to identify key links of the cyclone dynamical structure with the cloud fields. By combining these data, this study constructs a comprehensive qualitative picture of an archetypal extratropical cyclone in the Southern Hemisphere entirely from observations. It thereby significantly enhances previous studies that proposed conceptual models for these systems. In particular, our study expands analyses of extratropical cyclones carried out in earlier studies [*Field and Wood*, 2007; *Naud et al.*, 2010; *Bodas-Salcedo et al.*, 2012; *Booth et al.*, 2013] by analyzing the joint cloud and dynamical structure across the entire cyclone system and in all three dimensions. Drawing a quantitative rather than just qualitative picture of the cyclone structure leads to deeper insights into the working of cyclones as well as providing a more useful tool for model evaluation. Figures 4 and 5 and Table 1 showed that the relationship between cloud fraction, vertical motion, and relative humidity changes with height in observations. Consistent with results of *Bauer and DelGenio* [2006], ascent is confined to a smaller area and is stronger than descent in the composite cyclone. Higher values of cloud fraction are evident in the region of ascent, and the region of descent shows low values of cloud fraction at middle and high levels.

Figures 2 and 3 showed that the main characteristics of the constructed three-dimensional picture of a composite Southern Hemisphere extratropical cyclone includes thick, high top clouds in the warm frontal region, thin cirrus clouds just ahead of the warm frontal region, a small but still significant region of thick clouds in the cold frontal region, and low-level clouds at various depth almost everywhere in the cyclone

region. Thick and high "stormy" clouds are mainly present in the region of ascent and regions of higher relative humidity. Good vertical resolution of CloudSat/CALIPSO data is advantageous here to confirm that clouds are absent in the region of descent, except at low levels, where boundary clouds populate the composite cyclone.

The compositing method developed in this study provides a comprehensive approach to evaluate a climate model's ability to simulate clouds and dynamical processes in extratropical cyclones, in which cloud structures are invariably linked to the internal circulations. Given the large biases in the radiation budget in the models at the top of atmosphere, it is necessary to test the climate model's ability not only to accurately represent the cloud field in the right amount and at the correct location but also to represent the relationships between clouds and dynamical fields evident in the observations.

We evaluated the ACCESS model in this study as a test of our methodology. Figures 7 and 8 show that the model does not produce enough boundary layer clouds in extratropical cyclones. The relationship between cloud fraction and larger-scale dynamical variables in the model is not well reproduced. When measured by minimum pressure, the model has shallower cyclones than the observed. Consistent with findings of *Naud et al.* [2010], the circulation around the cyclone is weaker in the model and there is an underestimation of clouds in the western half of the system, in particular behind of the cold front region, while in the warm frontal region, the model produces too many clouds at very high levels compared with observations. The lack of clouds particularly at low levels in the model could explain *Trenberth and Fasullo's* [2010] finding that the absorbed shortwave radiation in the Southern Ocean is higher in the climate models than observed. The Southern Hemisphere is ocean dominated, and a lack of clouds in the model will cause an excess solar radiation at the ocean surface. There is a radiative bias of more than 40 W/m^2 behind the composite model cyclone center in the ACCESS model (not shown). The lack of clouds at middle and lower levels shown here very likely contributes to this large bias. This result is consistent with other models. *Bodas-Salcedo et al.* [2012] composited the shortwave CRE around cyclones for a version of the UK Met Office global model and showed that there is a large shortwave CRE bias in the cold air region.

The inability to simulate the correct dynamical structure of the composite cyclone makes it hard for the model to produce the correct cloud fields. It is of course not guaranteed that a better circulation will automatically lead to better cloud structures in the model. However the importance of the circulation for both moisture transport and diabatic processes is undisputed and makes the better representation of the circulation a clear prerequisite for simulating the right clouds for the right reasons.

6. Conclusions

This study has shown that compositing is a potent tool for investigating the structure of extratropical cyclones and their associated cloud fields and to assess the simulation of these features in climate models. CloudSat/CALIPSO data were used to extend the quasi two-dimensional view of extratropical cyclones in previous studies [*Lau and Crane*, 1995] to a truly three-dimensional perspective. The combination of these modern satellite cloud observations, objectively tracked cyclones and fronts, and supplementary reanalysis fields provides a consistent three-dimensional picture of a composite Southern Hemisphere extratropical cyclone.

Perhaps the most valuable aspect of our analysis is its use for the evaluation of climate models. Using the methodology developed here, we evaluated the ACCESS model for its ability to simulate the observed cloud and dynamical features and to reproduce the observed relationships between clouds and dynamical fields. The model is able to qualitatively reproduce the overall cloud structure around the cyclone center. However, it showed several shortcomings:

1. The circulation around the cyclone center is too weak.
2. The relationship between cloud fraction and larger-scale dynamical variables is not well reproduced. The model fails to show the observed quasi-linear relationship between cloud fraction and relative humidity.
3. The range of the dynamical variables in the composite model cyclone is smaller than observed.

Composite studies, like the one carried out here, are insufficient in themselves to clearly identify exactly what model changes need to be made. The latter requires more in-depth process studies likely involving individual cases. However, the three shortcomings listed above clearly show that the model simulation of

clouds in extratropical cyclones in the ACCESS models will require an effort beyond simple changes to the parametrizations, as the simulation of the dynamical state of the cyclone is also poor.

It would be interesting to see if any of these model outputs alter with use of the COSP simulator for model simulation. Using the methodology developed here, comparison between different models or comparison between many versions of any model is easily possible. Furthermore, it would be interesting to perform model sensitivity studies, such as changes to the model resolution or model parameter settings to identify possible areas of model improvement.

The methodology developed here links dynamics with cloud field in the cyclone. Clearly, there remain large errors related to clouds in climate models which must be addressed in order to have confidence in future projection of the Earth's climate. A natural extension of the work presented here is the application of the methodologies to the large climate model ensemble collected by the CMIP5 project [*Taylor*, 2012], to gain a comprehensive understanding of modern climate models' ability to simulate Southern Ocean cyclones.

Acknowledgments

The data used for this study are available online at http://cloudsat.atmos.colostate.edu and http://www.esrl.noaa.gov/psd/data/. This study was supported by the Australian Research Council through the Linkage Project grant LP0883961, the Discovery Project grant DP0877417, the ARC Centre of Excellence for Climate System Science (CE110001028), and the ARC DECRA (DE140101305). The authors thank the Editor and the three anonymous reviewers for suggestions that improved the manuscript. We thank Gareth Berry for providing data for fronts.

References

Bauer, M., and A. D. DelGenio (2006), Composite analysis of winter cyclones in a GCM: Influence on climatological humidity, *J. Clim.*, *19*, 1652–1672.

Berry, G., M. J. Reeder, and C. Jakob (2011), A global climatology of atmospheric fronts, *Geophys. Res. Lett.*, *38*, L04809, doi:10.1029/2010GL046451.

Betts, A. K., M. Zhao, P. A. Dirmeyer, and A. C. M. Beljaars (2006), Comparison of ERA40 and NCEP/DOE near-surface data sets with other ISLSCP-II data sets, *J. Geophys.Res.*, *111*, D22S04, doi:10.1029/2006JD007174.

Bjerknes, J., and H. Solberg (1922), Life cycle of cyclones and the polar front theory of atmospheric circulation, *Geophysisks Publikationer*, *3*, 18.

Bodas-Salcedo, A., et al. (2011), COSP: Satellite simulation software for model assessment, *Bull. Am. Meteorol. Soc.*, *92*(8), 1023–1043.

Bodas-Salcedo, A., K. Williams, P. Field, and A. Lock (2012), The surface downwelling solar radiation surplus over the Southern Ocean in the Met Office model: The role of midlatitude cyclone clouds, *J. Clim.*, *25*, 7467–7486.

Bony, S., R. Colman, V. M. Kattsov, R. P. Allan, C. S. Bretherton, J. Dufresne, and A. Hall (2006), How well do we understand and evaluate climate change feedback processes of climate, *J. Clim.*, *19*, 3445–3482.

Booth, J. F., C. M. Naud, and A. D. D. Genio (2013), Diagnosing warm frontal cloud formation in a GCM: A novel approach using conditional subsetting, *J. Clim.*, *26*, 5827–5845.

Browning, K. A., and N. M. Roberts (1994), Structure of a frontal cyclone, *Q. J. R. Meteorolog. Soc..*, *120*, 1535–1557.

Catto, J. L., L. C. Shaffery, and K. I. Hodges (2010), Can climate models capture the structure of extratropical cyclones?, *J. Clim.*, *23*, 1621–1635.

Ceppi, P., Y. T. Hwang, D. M. W. Frierson, and D. L. Hartmann (2012), Southern Hemisphere jet latitude biases in CMIP5 models linked to shortwave cloud forcing, *Geophys. Res. Lett.*, *39*, L19708, doi:10.1029/2012GL053115.

Cess, R. D., et al. (1990), Intercomparison and interpretation of climate feedback processes in 19 atmospheric general circulation models, *J. Geophy. Res.*, *95*, 16,601–16,615.

Chang, E. K. M., and S. W. Song (2006), The seasonal cycles in the distribution of precipitation around cyclones in the western North Pacific and Atlantic, *J. Atmos. Sci.*, *63*, 815–839.

Collins, W., et al. (2008), Evaluation of the HadGEM2-ES model, *Hadley Centre Technical Note 47*, 48, Met Office Hadley Centre, Exter, U. K. [Avialable at http://www.metoffice.gov.uk/research/hadleycentre/pubs/HCTN/index.html.]

Field, P., and R. Wood (2007), Precipitation and cloud structure in midlatitude cyclones, *J. Clim.*, *20*, 233–254.

Field, P., A. Gettelman, R. Neale, R. Wood, P. Rasch, and H. Morrison (2008), Midlatitude cyclone compositing to constrain climate model behaviour using satellite observations, *J. Clim.*, *21*, 5887–5903.

Field, P. R., A. Bodas-Salcedo, and M. E. Brooks (2011), Using model analysis and satellite data to assess cloud and precipitation in midlatitude cyclones, *Q. J. R. Meteorol. Soc.*, *137*, 1501–1515.

Frierson, D. M. W., and Y. T. Hwang (2012), Extratropical influence on ITCZ shifts in slab ocean simulations of global warming, *J. Clim.*, *25*, 720–733.

Govekar, P. D., C. Jakob, M. J. Reeder, and J. Haynes (2011), The three-dimensional distribution of clouds around Southern Hemisphere extratropical cyclones, *Geophy. Res. Lett.*, *38*, L21805, doi:10.1029/2011GL049091.

Haynes, J. M., T. S. L'Ecuyer, G. L. Stephens, S. D. Miller, C. Mitrescu, N. B. Wood, and S. Tanelli (2009), Rainfall retrieval over the ocean with spaceborne W-band radar, *J. Geophys. Res.*, *114*, D00A22, doi:10.1029/2008JD009973.

Haynes, J. M., C. Jakob, W. B. Rossow, G. Tselioudis, and J. Brown (2011), Major characteristics of Southern Ocean cloud regimes and their effects on the energy budget, *J. Clim.*, *24*, 5061–5080.

Hwang, Y. T., and D. M. W. Frierson (2013), Link between the double-intertropical convergence zone problem and cloud biases over the Southern Ocean, *Proc. Natl. Acad. Sci. U.S.A.*, *110*, 4935–4940, doi:10.1073/pnas.121302110.

Jiang, J. H., et al. (2012), Evaluation of cloud and water vapor simulations in CMIP5 climate models using NASA "A-Train" satellite observations, *J. Geophys. Res.*, *D14*, D14105, doi:10.1029/2011JD017237.

Klein, S., and C. Jakob (1999), Validation and sensitivities of frontal clouds simulated by the ECMWF model, *Mon. Weather Rev.*, *127*, 2514–2531.

Lau, N. C., and M. W. Crane (1995), A satellite view of the synoptic-scale organization of cloud properties in midlatitude and tropical circulation systems, *Mon. Weather Rev.*, *123*, 1984–2006.

Lau, N. C., and M. W. Crane (1997), Comparing satellite and surface observations of cloud patterns in synoptic-scale circulation systems, *Mon. Weather Rev.*, *125*, 3172–3189.

Lauer, A., K. Hamilton, Y. Wang, V. Phillips, and R. Bennartz (2010), The impact of global warming on marine boundary layer clouds over the Eastern Pacific—A regional model study, *J. Clim.*, *23*, 5844–5863.

Mace, G. G. (2010), Cloud properties and radiative forcing over the maritime storm tracks of the Southern Ocean and North Atlantic derived from A-Train, *J. Geophys. Res.*, *115*, D00A26, doi:10.1029/2009JD012517.

Mace, G. G., Q. Zhang, M. Vaughan, R. Marchand, G. Stephens, C. Trepte, and D. Winker (2009), A desription of hydrometeor layer occurrence statistics derived from the first year of merged Cloudsat and CALIPSO data, *J. Geophys. Res.*, *114*, D00A26, doi:10.1029/2007JD009755.

Marchand, R., G. G. Mace, T. Ackerman, and G. Stephens (2008), Hydrometeor detection using CloudSat—An Earth-orbiting 94-GHz cloud radar, *J. Atmos. Oceanic Technol.*, *25*, 519–533.

Naud, C. M., A. D. DelGenio, M. Bauer, and W. Kovari (2010), Cloud vertical distribution across warm and cold fronts in Cloudsat-CALIPSO data and a general circulation model, *J. Clim.*, *23*, 3397–3415.

Naud, C. M., D. Posselt, and S. van den Heever (2012), Observational analysis of cloud and precipitation in midlatitude cyclones: Northern versus Southern Hemisphere warm fronts, *J. Clim.*, *25*, 5135–5151.

Neiman, P. J., M. A. Shapiro, and L. S. Fedor (1993), The life cycle of an extratropical marine cyclone, part II: Mesoscale structure and dignostics, *Mon. Weather Rev.*, *121*, 2177–2199.

Norris, J. R., and S. F. Iacobellis (2005), North Pacific cloud feedbacks inferred from synoptic-scale dynamic and thermodynamic relationship, *J. Clim.*, *18*, 4862–4878.

Norris, J. R., and C. P. Weaver (2001), Improved techniques for evaluating GCM cloudiness applied to the NCAR CCM3, *J. Clim.*, *14*, 2540–2550.

Posselt, D., G. Stephens, and M. Miller (2008), Cloudsat—Adding a new dimension to a classical view of extratropical cyclones, *Bull. Amer. Meteor. Soc.*, *89*, 599–609.

Rudeva, I., and S. K. Gulev (2011), Composite analysis of north Atlantic extratropical cyclones in the NCEP reanalysis data, *Mon. Weather Rev.*, *139*, 1419–1446.

Sanderson, B. M., C. Piani, W. J. Ingram, D. A. Stone, and M. R. Allen (2008), Towards constraining climate sensitivity by linear analysis of feedback patterns in thousands of perturbed-physics GCM simulations, *Clim. Dyn.*, *30*, 175–190.

SenGupta, A., A. Santoso, A. Taschetto, C. C. Ummenhofer, J. Trevena, and M. H. England (2009), Projected changes to the Southern Hemisphere Ocean and sea ice in the IPCC AR4 climate models, *J. Clim.*, *22*, 3047–3078.

Simmonds, I., and K. Keay (2000), Mean Southern Hemisphere extratropical cyclone behaviour in the 40-year NCEP-NCAR reanalysis, *J. Clim.*, *13*, 873–885.

Slingo, J. M. (1997), The development and verification of a cloud prediction scheme for the ECMWF model, *Q. J. R. Meteorolog. Soc.*, *113*, 899–927.

Stephens, G. L., et al. (2002), The Cloudsat mission and the A-TRAIN: A new dimension to space-based observations of clouds and precipitation, *Bull. Am. Meteorol. Soc.*, *83*, 1771–1790.

Su, H., J. H. Jiang, J. Teixeira, A. Gettelman, X. Huang, G. Stephens, D. Vane, and V. S. Perun (2011), Comparison of regime-sorted tropical cloud profiles observed by CloudSat with GEOS5 analyses and two general circulation model simulations, *J. Geophys. Res.*, *116*, D09104, doi:10.1029/2010JD014971.

Taylor, K. E. (2012), An overview of CMIP5 and the experiment design, *Bull. Amer. Meteor. Soc.*, *93*, 485–498.

Trenberth, K. E. (1991), Storm tracks in the Southern Hemisphere, *J. Atmos. Sci.*, *48*, 2159–2178.

Trenberth, K. E., and J. Fasullo (2010), Simulation of present day and 21st century energy budgets of the southern oceans, *J. Clim.*, *23*, 440–454.

Tsushima, Y., et al. (2006), Importance of the mixed-phase cloud distribution in the control climate for assessing the response of clouds to carbon dioxide increase: A multi-model study, *Clim. Dyn.*, *27*, 113–126.

Webb, M., C. Senior, S. Bony, and J. J. Morcrette (2001), Combining ERBE and ISCCP data to assess clouds in the Hadley Centre, ECMWF and LMD atmospheric climate models, *Clim. Dyn.*, *17*, 905–922.

Williams, K. D., et al. (2013), The transpose-AMIP II experiment and its application to the understanding of Southern Ocean cloud biases in climate models, *J. Clim.*, *26*, 3258–3274.

Wilson, D. R., A. C. Bushell, A. M. Kerr-Munslow, D. Price, and C. Morcrette (2008), A prognostic cloud fraction and condensation scheme. Part I: Scheme description, *Q. J. R.Meteorol. Soc.*, *134*, 2093–2107.

Winker, D., W. H. Hunt, and M. J. McGill (2007), Initial performance assesssment of CALIOP, *Geophys. Res. Lett.*, *34*, L19803, doi:10.1029/2007GL030135.

Zhou, C., M. Zelinka, A. Dessler, and P. Yang (2013), An analysis of the short-term cloud feedback using MODIS data, *J. Clim.*, *26*, 4803–4815.